$\mathcal{PT}$-Symmetric Coupled-Resonator Waveguide Based on Buried Heterostructure Nanocavities

Kenta Takata and Masaya Notomi
Nanophotonics Center, NTT Corporation, 3-1 Morinosato-Wakamiya, Atsugi 243-0198, Kanagawa, Japan
and NTT Basic Research Laboratories, NTT Corporation, 3-1 Morinosato-Wakamiya,
Atsugi 243-0198, Kanagawa, Japan
(Received 15 February 2017; published 26 May 2017)

We propose and theoretically study a parity-time ($\mathcal{PT}$)-symmetric photonic-crystal coupled-resonator optical waveguide (CROW) based on buried heterostructure nanocavities which has potential scalability and controllability. We analytically reveal its spectral transport properties with a tight-binding model and show the possibility of the wide-range control of its group velocity using the $\mathcal{PT}$ phase transition. While the group velocity at the $\mathcal{PT}$ phase-transition point diverges, the group-velocity dispersion converges. A numerical estimation of the system response to temporal pulse inputs shows that the pulse broadening is not severe in a device of hundreds of micrometers in size. Furthermore, a longer pulse duration results in a higher upper limit of the pulse peak velocity, which can be, in principle, superluminal. We next perform numerical simulations on the considered photonic-crystal slab structures with the finite-element method, and we successfully observe $\mathcal{PT}$ phase transitions. In the simulated parameter range, gain and loss coefficients of the order of 100 cm^{-1} meet the condition for the maximum group-velocity coefficient in the context of the tight-binding approach. A 9.3-fold increase in the group velocity at 1502 nm is obtained in a three-dimensional device by switching between the conventional and $\mathcal{PT}$-symmetric CROWs. Meanwhile, we also encounter band smoothing around the phase transition, which hampers the group-velocity divergence. Our simulation result indicates that it arises from interfering evanescent waves decaying out of the device structure, and we discuss ways to suppress this effect.

DOI: 10.1103/PhysRevApplied.7.054023

I. INTRODUCTION

It has been a long-standing goal to fully control the speed of light in photonic devices. With respect to slowing the light, an array of optical microcavities with evanescent coupling, called a coupled-resonator optical waveguide (CROW) [1,2], is one of the most promising platforms. In such a system, the confinement of photons in cavities and their limited tunneling give their effective mass, and hence a gentle cosine-shaped photonic band curve. As a result, a CROW can achieve an optical group velocity orders of magnitude smaller than the speed of light in vacuum and a negligible group-velocity dispersion at the band center. Applications such as a compact optical delay line [3], enhancement of the nonlinear optical effect [4] and mode locking [5,6] have been proposed. Also, the number of coherently coupled resonators in the experimental demonstration has been extended to over one thousand, which amounts to as long as 1 mm in terms of device length [7]. Here, the practical challenge is to significantly tune their optical response with external signals.

To realize optical devices with extra controllability and functionality, an emerging feature in artificial dielectric structures with balanced gain and loss has recently been studied. It originates from a quantum-mechanical concept, known as parity-time ($\mathcal{PT}$) symmetry [8], in which the system Hamiltonian is invariant to the parity- ($\hat{\mathcal{P}}$) and time- ($\hat{\mathcal{T}}$) reversal operation set. It has suggested an exotic class of systems that retain their real, and hence their observable energy eigenvalues, even in the presence of partial non-Hermitian factors such as amplification and dissipation. In addition, it is known that its protection of quasi-Hermiticity is not always perfect, meaning that increasing the imaginary potential can induce a phase transition from real to imaginary eigenvalues. Because of the correspondence between the Schrödinger equation and the paraxial wave equation, classical optics has been suggested as a good test bed for $\mathcal{PT}$ symmetry and its symmetry breaking [9–11]. A certain condition is required for the complex refractive index $n(\mathbf{r}) = n^*(-\mathbf{r})$, meaning that its real part has an even spatial parity, while the imaginary part is an odd function, thereby leading to $\mathcal{PT}$ symmetry. Various interesting phenomena have already been observed in such systems, for example, power oscillation [9,12], double refraction [9], unidirectional reflectivity [13,14], and single-mode lasing [15,16]. Here, large $\mathcal{PT}$-symmetric waveguide arrays in the time domain have been reported [12,17]; however, practical demonstrations using spatial gain and loss structures are still challenging in terms of scale or gain control.

$\mathcal{PT}$-symmetric CROWs have both strong light confinement and optical gain and loss in their constituent cavities. Thus, their non-Hermitian structures, along with the propagation direction, greatly affect their dispersion relation, and hence their group velocity. A theoretical analysis [18] shows that large systems can show significant unidirectional

reflectivity and transmission restriction. Furthermore, a non-Hermitian CROW is expected to show the divergence of its group velocity due to an exceptional point [19]. However, experimental realization of such theoretical bulk features has not been extensively pursued. Demonstrations are still limited to two coupled high-Q microtoroid resonators [20,21] showing nonlinearity-induced isolation, which need optical pumping and fine-tuning of their positions, and hence coupling.

In this paper, we propose and study theoretically an alternative $\mathcal{PT}$-symmetric CROW based on photonic-crystal buried heterostructure mode-gap (BHM) nanocavities [22–24], which will have both experimental scalability and gain controllability. We first illustrate the device and describe it with a coupled-mode equation corresponding to the tight-binding model. Here, we derive the input frequency dependences of its group velocity and group-velocity dispersion, which are of practical importance. They show that the group velocity diverges at the phase-transition frequency, while the group-velocity dispersion converges. This feature suggests that the switching from the slow light transport of a conventional CROW to fast light transport in a $\mathcal{PT}$-symmetric CROW might be realized by external pumping control. The result also clarifies that the optimum group velocity and group-velocity dispersion can be estimated by the cavity coupling and cavity spatial interval of a given conventional CROW without gain and loss. This fact supports the advantage of our system based on compact and then strongly coupling nanocavities. Next, we perform a numerical analysis of the temporal system response to pulse inputs. Our analysis shows that the fundamental upper limit of the pulse peak velocity depends on the input pulse width, although the system might allow superluminal propagation. Furthermore, propagation in the device of over 200 μm does not significantly broaden input pulses with durations of tens of picoseconds. Finally, we simulate realistic device structures composed of photonic-crystal nanocavities with complex refractive indices and examine their band structures. Here, the $\mathcal{PT}$ phase transition is successfully observed assuming realistic gain-coefficient values. The simulated band curves are reproduced by a theoretical model that includes up to the second-nearest-neighbor coupling, where the coupling rates can be estimated with moderate data points. However, we observed the smoothing of the exceptional-point singularity [25]. It can lead to a small available group velocity and can impede possible exotic phenomena based on the $\mathcal{PT}$ phase transition. Our result suggests that this is because of the interfering light radiating out of the structure, which can be modeled by a small imaginary part of the cavity-cavity coupling [26]. Here, a high system Q factor is shown to be essential to obtain a large group velocity. Our structure tuning achieves a 9.3-fold increase in the velocity by switching between the conventional and $\mathcal{PT}$-symmetric CROWs in three dimensions.

The remainder of this paper is organized as follows. In Sec. II, we describe the device proposed in this study. Section III shows theoretical transport properties of the system based on the tight-binding approach. Section IV provides the result of a numerical simulation of realistic photonic-crystal structures. Section V discusses the trade-off between the possible group velocity and the required gain and loss. It also mentions ways to recover the singularity in imperfect systems. Section VI concludes the paper.

II. $\mathcal{PT}$-SYMMETRIC CROW BASED ON BURIED HETEROSTRUCTURE NANOCAVITIES

In this section, we describe the device structure proposed in this study. Figure 1(a) shows the structure schematically. The system is composed of a semiconductor photonic-crystal slab, a line defect, BHM nanocavities along with the line defect, and an appropriate pumping mechanism for each cavity. The photonic-crystal structure is omitted from Fig. 1(a) for simplicity. A periodic gain and loss profile is realized by electrical or optical pumping in BHM cavities. Figure 1(a) shows the case for electrical pumping. Here, the green and purple parts in the semiconductor slab are p doped and n doped, respectively, for each independent current-injection channel to control gain and loss in each cavity. The red (blue) rectangular BHM nanocavities indicate their gain by the current injection (loss by the material absorption). Closely placed nanocavities give large cavity coupling rates, which result in the CROW bandwidth of $\gtrsim$1 nm. Figure 1(b) shows the complex refractive-index profile along with the center of the line defect. Here, each BHM works as a cavity due to a sharp index modulation and, at the same time, induces gain or loss [a finite Im(n)] as a result of pumping and intrinsic material absorption.

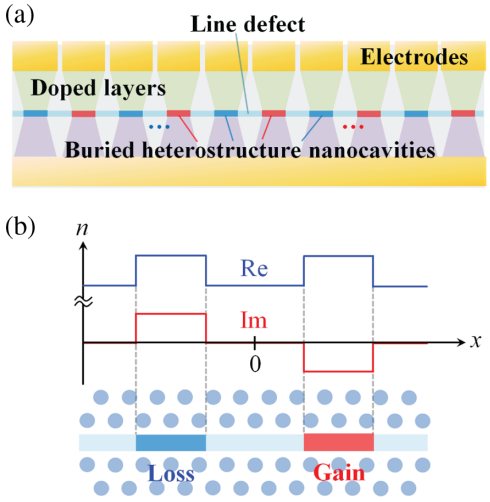

FIG. 1. (a) Schematic of the proposed $\mathcal{PT}$-symmetric CROW with electrical pumping. (b) The refractive-index profile along with the line defect and the array of BHM cavities.

When we use the x axis at the center of the BHM cavity array as a reference, $\mathrm{Re}(n)$ is even in x and $\mathrm{Im}(n)$ is odd. Thus, the system guarantees the existence of $\mathcal{PT}$ symmetry for suitable amounts of equal gain and loss.

III. THEORETICAL ANALYSIS WITH A TIGHT-BINDING MODEL

A. Theoretical model

For a theoretical analysis of the system, we consider a simplified coupled-mode-equation analysis equivalent to the tight-binding model illustrated in Fig. 2(a). Here, each cavity mode is described by the slowly varying electric-field amplitude $E_m(t)$, where m is the cavity index. The system comprises N pairs of cavities with alternating loss and gain, and the periodic boundary is set by the perfect electric conductors at its edges, requiring $E_0 = E_{2N+1} = 0$. The real part of the local index for each BHM cavity n_{BH} is assumed to be constant, whereas its imaginary part varies depending on whether the cavity undergoes gain ($+g$) or loss ($-g$). The cavities are evanescently coupled and their real coupling coefficient is expressed by κ. The spatial interval of the cavities L_{CC} affects the transport properties estimated later. Note that the period of identical unit cells is $2L_{\mathrm{CC}}$, namely, a pair of cavities with gain and loss. Thus, the cosinusoidal band structure of the conventional empty CROW ($g = 0$) is folded in half, as shown in Fig. 2(b). We obtain some device parameters, such as $\kappa = 2 \times 10^{-3}$ and $L_{\mathrm{CC}} = 2.1\ \mu$m, from Ref. [3]. The equation of motion for each field amplitude can be described as a series of temporal coupled-mode equations [27,28],

$$\frac{dE_m}{dt} = -\frac{\omega_0}{2Q}E_m + \frac{g_m c}{2n_{\mathrm{BH}}}E_m - i\frac{\kappa\omega_0}{2}(E_{m+1} + E_{m-1}). \quad (1)$$

Here, ω_0 is the single-cavity resonance frequency, which equals the frequency of the rotating frame, Q is the cavity quality factor and $\omega_0/(2Q)$ is the cavity decay rate. c is the speed of light in vacuum and $g_m c/(2n_{\mathrm{BH}})$ is the gain and loss rate in term of photons with the local phase velocity in each cavity. We combine the first and second terms in Eq. (1) and define the cavity-index-dependent coefficient g_m for E_m as follows:

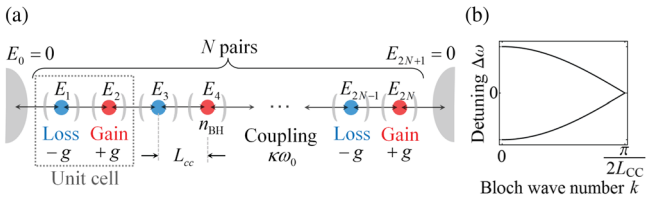

FIG. 2. (a) Illustration of the theoretical model for the $\mathcal{PT}$-symmetric CROW. (b) Sketch of the half-folded band structure of the conventional CROW ($g = 0$) with a spatial period of $2L_{\mathrm{CC}}$.

$$g_m = \begin{cases} g + \frac{n_{\mathrm{BH}}\omega_0}{cQ} & (m \text{ is even}), \\ -g + \frac{n_{\mathrm{BH}}\omega_0}{cQ} & (m \text{ is odd}). \end{cases} \quad (2)$$

This means that the single-cavity decay is just a linear term in Eq. (1) and hence can be canceled by the controlled gain and loss. $g > 0$ is the net gain (even m) and loss (odd m) coefficient for the considered cavity mode. We also assume that a large part of the field decay works as photonic tunneling (evanescent coupling) between the cavities. Thus, the coupling rate is sufficiently large compared to the decay rate. The device can then be regarded as a large coherently coupled cavity system, and its total gain and loss are balanced. Therefore, $\mathcal{PT}$ symmetry will be realized without lasing, as in previous studies [20,21], and we focus on the linear $\mathcal{PT}$-symmetric system with regard to the gain and loss terms. Note that g parametrizes various factors, such as mode confinement, carrier dynamics, and gain saturation.

After substituting Eq. (2) into Eq. (1), we find that the resultant field equation corresponds to the Schrödinger equation of a non-Hermitian tight-binding model [18],

$$i\frac{d\Psi_m}{dt} = ig'_m\Psi_m + \kappa'(\Psi_{m+1} + \Psi_{m-1}), \quad (3)$$

with simplification,

$$\kappa' = \frac{1}{2}\kappa\omega_0,$$
$$g'_m = \begin{cases} \frac{gc}{2n_{\mathrm{BH}}} = g' & (m \text{ is even}), \\ -\frac{gc}{2n_{\mathrm{BH}}} & (m \text{ is odd}), \end{cases} \quad (4)$$

where we have changed the notation of the field $E_m \to \Psi_m$ for visual correspondence. With the ansatz for the differential equation $\Psi_m(t) = \exp(-i\Delta\omega t)\psi_m$, we obtain the eigenvalue equation for the frequency detuning $\Delta\omega$,

$$\Delta\omega\psi_m = ig'_m\psi_m + \kappa'(\psi_{m+1} + \psi_{m-1}). \quad (5)$$

Here, the reference for $\Delta\omega$ in the rotating frame is the resonance frequency ω_0.

B. Complex band structure with nearest-neighbor coupling

The eigenvalues of Eq. (5) can be derived by using the Bloch theorem [18],

$$\Delta\omega(K_s) = \pm\sqrt{4\kappa'^2\cos^2 K_s - g'^2}, \quad (6)$$

where the eigenstates require Bloch phase factors with discrete values,

$$K_s = \frac{s\pi}{2N+1}\ (s = 1, \ldots, N). \quad (7)$$

Note that K_s is dimensionless and that the wave number is $K_s/L_{CC} < \pi/(2L_{CC})$. The negative K_s case is omitted for simplicity. The effect of the gain and loss shows up as $-g'^2$ in the square root of Eq. (6), and it enables the eigenvalues to be purely imaginary. Here, the shape of the band structure does not depend on N. We hence focus on $N \to \infty$, leading to band curves formed by the continuum of eigenstates ($K_s \to kL_{CC} \in \mathbb{R}$, where k is the Bloch wave number). Figures 3(a) and 3(b) show the real and imaginary eigenfrequency detuning $\Delta\omega(k)$ for different magnitudes of the net gain and loss, $g = 0, 200, 405, 500$ cm^{-1}. The black curves give the folded cosine-shaped band structure of the empty CROW. When g is finite, the two real branches coalesce inside the first Brillouin zone, and nondegenerate imaginary branches appear. The point with $\mathrm{Re}(\Delta\omega) = \mathrm{Im}(\Delta\omega) = 0$ is hence called the $\mathcal{PT}$ phase-transition point, or the exceptional point, and it induces switching from extended CROW modes to a pair of amplifying and deamplifying modes localized in the gain and loss parts. Comparing different curves, we see that as g increases by hundreds of cm^{-1}, the transition point moves largely toward the inside of the band for the set of parameters considered. Many exotic and interesting phenomena occur around this exceptional point, and here we pay attention to the divergence of the group velocity, namely, the gradient of the real branches.

C. Group velocity and group-velocity dispersion

Here, we theoretically clarify the transport properties of the $\mathcal{PT}$-symmetric CROW with the tight-binding model. First, differentiation of $\Delta\omega(k)$ and variable transformation give the spectral group velocity. For the lower branch before the phase transition, the analytical expression is

$$v_g(\Delta\omega) = \frac{d\Delta\omega}{dk} = L_{CC}\frac{d\Delta\omega}{dK_s} = -\frac{L_{CC}}{\Delta\omega}\sqrt{(\Delta\omega^2 + g'^2)(4\kappa'^2 - \Delta\omega^2 - g'^2)} \quad (\Delta\omega < 0). \tag{8}$$

Equation (8) for different gain and loss coefficients is plotted in Fig. 4(a). Here, $\Delta\omega = 0$ indicates the phase-transition point, as seen in Fig. 3(a). Clear divergence of the curves for finite g's due to $1/\Delta\omega \to \infty(\Delta\omega \to 0)$ in Eq. (8) is observed. On the other hand, the group velocity for the empty CROW ($g = 0$) is finite and small at $\Delta\omega = 0$, meaning that a great change is induced in v_g by the introduction of the $\mathcal{PT}$

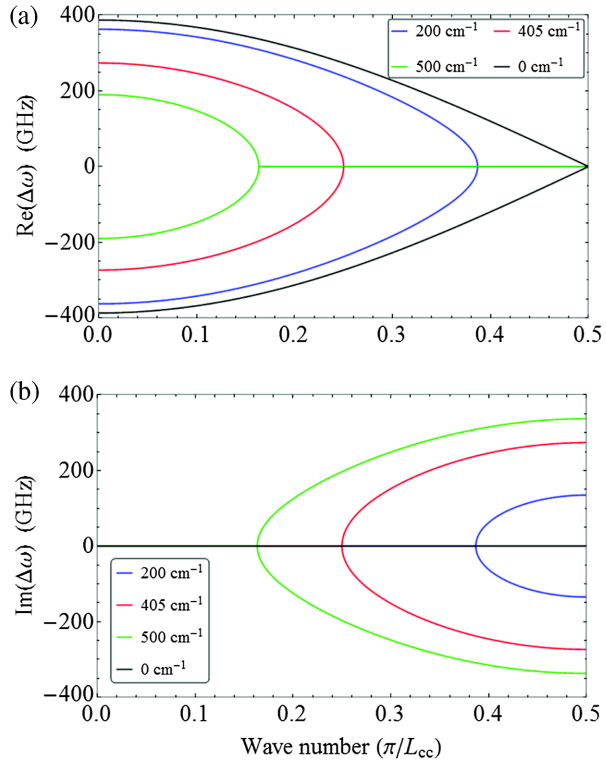

FIG. 3. (a) Real and (b) imaginary parts of the eigenfrequency detuning in the $\mathcal{PT}$-symmetric CROW for different gain and loss rates g. $n_{BH} = 3.54$, $\lambda_0 = c/\omega_0 = 1.55$ μm, $\kappa = 2 \times 10^{-3}$. The curve for $g = 405$ cm^{-1} in (a) is a parabola with the longest focal length and hence the largest group-velocity coefficient, satisfying Eq. (10).

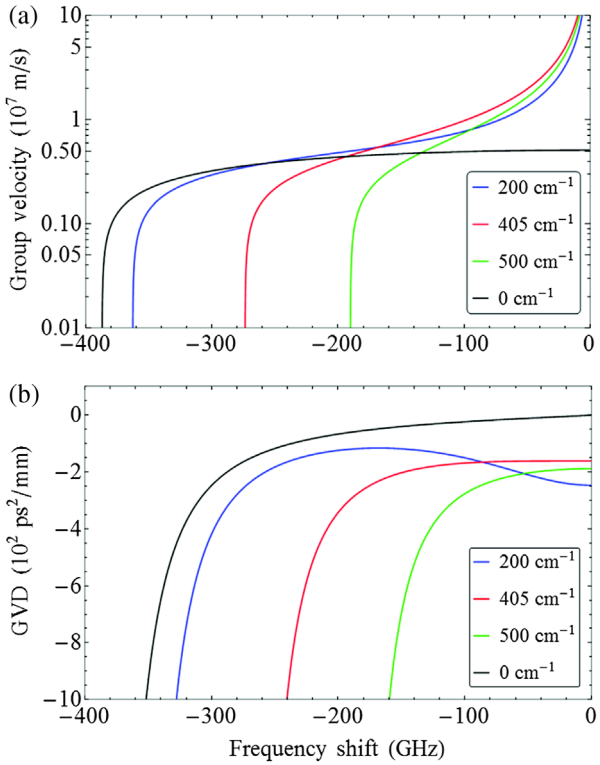

FIG. 4. (a) The spectral group velocity and (b) the group-velocity dispersion of the $\mathcal{PT}$-symmetric CROW for different gain and loss rates. $n_{BH} = 3.54$, $\lambda_0 = 2\pi c/\omega_0 = 1.55$ μm, $\kappa = 2 \times 10^{-3}$. The curve for $g = 405$ cm^{-1} in (b) gives the minimum $|\mathrm{GVD}(\Delta\omega = 0)|$ in a finite g.

phase transition. We can easily obtain the asymptotic behavior of v_g from Eq. (8) for $\Delta\omega \approx 0$,

$$v_g \to -\frac{L_{CC}}{\Delta\omega}\sqrt{g'^2(4\kappa'^2 - g'^2)} = -\frac{L_{CC}}{\Delta\omega}\sqrt{-(g'^2 - 2\kappa'^2)^2 + 4\kappa'^4}. \quad (9)$$

We then find that the condition for the largest v_g around the transition point is

$$g' = \sqrt{2}\kappa'. \quad (10)$$

With this relation, the continuous solution of Eq. (6) for $\Delta\omega = 0$ is $k = \pi/(4L_{CC})$. This means that the highest group velocity is obtained when the transition occurs at the middle of the band for $k > 0$. The plot for v_g with $g = 405\ \mathrm{cm}^{-1}$ in Fig. 3(a) actually meets this condition [Eq. (10)]. Therefore, the curve with $g = 405\ \mathrm{cm}^{-1}$ in Fig. 4(a) is uppermost for $\Delta\omega \approx 0$ of the four g values. The resultant coefficient in Eq. (9) with Eq. (10) is $2L_{CC}\kappa'^2 = L_{CC}\kappa^2\omega_0^2/2$, which is proportional to both the cavity period L_{CC} and the square of the coupling factor κ^2. By contrast, the group velocity for the empty CROW at $\Delta\omega = 0$ is $v_{g,\mathrm{empty}} = 2\kappa' L_{CC} = \kappa\omega_0 L_{CC}$. Thus, around the transition point ($\Delta\omega \approx 0$), $v_g/v_{g,\mathrm{empty}} \approx \kappa\omega_0/(2\Delta\omega)$, showing linear enhancement of the velocity ratio with the coupling coefficient κ. As shown previously [3], κ decays exponentially with L_{CC}. A smaller L_{CC} thus leads to a larger v_g for the light near the exceptional point.

Next, we examine the group-velocity dispersion (GVD), which characterizes the pulse broadening. GVD is defined as the spectral gradient of the group delay for unit propagation distance and is derived with Eq. (8),

$$\mathrm{GVD}(\Delta\omega) = \frac{d}{d\Delta\omega}\left(\frac{1}{v_g}\right) = \frac{-\Delta\omega^4 - 4g'^2\kappa'^2 + g'^4}{L_{CC}[(\Delta\omega^2 + g'^2)(4\kappa'^2 - \Delta\omega^2 - g'^2)]^{3/2}} \quad (\Delta\omega < 0). \quad (11)$$

The data obtained with Eq. (11) for different g values are displayed in Fig. 4(b). An empty CROW ($g = 0$) does not suffer from any GVD around $\Delta\omega = 0$. On the other hand, the gain and loss result in a finite GVD in $\mathcal{PT}$-symmetric CROWs. It diverges under large negative frequency detuning (flatband regime), while it converges at the transition point because $v_g(\Delta\omega \approx 0) \propto 1/\Delta\omega$. Here, the spectral width of the region with a small |GVD| depends on $4\kappa'^2 - g'^2$. The magnitude of the GVD at the transition point for a finite g' can be obtained as

$$|\mathrm{GVD}(\Delta\omega = 0)| = \frac{1}{L_{CC}\sqrt{-(g'^2 - 2\kappa'^2)^2 + 4\kappa'^4}}. \quad (12)$$

We see that the condition for the smallest $|\mathrm{GVD}(\Delta\omega = 0)|$ is the same as Eq. (10). The consequent minimum |GVD| is $1/(2L_{CC}\kappa'^2) = 2/(L_{CC}\kappa^2\omega_0^2)$, which is the inverse of the maximum coefficient of v_g for $\Delta\omega \approx 0$. Again, a shorter L_{CC} leads to an exponentially larger κ, and hence smaller pulse broadening, depending on $1/\kappa^2$. Note that the curve of $g = 405\ \mathrm{cm}^{-1}$ in Fig. 4(b) shows the smallest GVD around $\Delta\omega = 0$ when the gain and loss rates are nonzero. Overall, we can estimate the possible group velocity and group-velocity dispersion in a $\mathcal{PT}$-symmetric CROW from the device parameters of its conventional counterpart $\{\kappa, \omega_0, L_{CC}\}$ with no gain or loss introduced. Available values of κ' and L_{CC} in in-line coupled photonic-crystal nanocavities are 200 GHz and 2 μm [3], while those for microtoroid resonators, which are also good for $\mathcal{PT}$-symmetric systems, can be 1 GHz and 60 μm [20,21]. Thus, the optimum coefficient of v_g and $1/|\mathrm{GVD}|$ is larger by two orders of magnitude in photonic-crystal systems. This difference shows the advantage of our device in terms of achieving fast light transport.

D. Estimation of the temporal response

We have already studied analytically the group velocity and group-velocity dispersion of the system, along with their parameter dependence. Here, we provide a numerical estimation of the temporal response of the bulk system to a pulse running over a finite distance. As shown in Fig. 3, the band structure of the system is nonlinear and hence will lead to non-negligible high-order dispersion. Therefore, a pulse with a broad spectral distribution can show propagation slower than that with the theoretical group velocity. The dependence of the response on the input pulse duration will hence be of significant importance. We take these factors into account and show the upper limit of the pulse peak velocity. In addition, the finite length of the system limits the temporal delay of propagating optical pulses. Thus, we see whether a detectable temporal shift of the pulses are obtained by switching between empty and $\mathcal{PT}$-symmetric CROWs over a moderate propagation distance.

The evolving pulse amplitude at cavity site m, $\Phi(m,t)$ is expressed by the Fourier integral of the Bloch-Floquet eigenmodes $\psi_{\pm,m}(k)$, including their wave-number spectral functions $F_\pm(k)$ and phase rotations [19,29]. For our system with a period of two cavities, the pulse amplitude is given by

$$\Phi(m,t) = \int_{-\pi/(2L_{CC})}^{\pi/(2L_{CC})} dk F_+(k)\psi_{+,m}(k) \times \exp\left[i2kL_{CC}\left\lfloor\frac{m}{2}\right\rfloor - i\Delta\omega_+(k)t\right] + \int_{-\pi/(2L_{CC})}^{\pi/(2L_{CC})} dk F_-(k)\psi_{-,m}(k) \times \exp\left[i2kL_{CC}\left\lfloor\frac{m}{2}\right\rfloor - i\Delta\omega_-(k)t\right], \quad (13)$$

where the subscript $\{+,-\}$ corresponds to the sign of the eigenfrequency detuning $\Delta\omega(k)$ [see Eq. (6)], and

$$\psi_{\pm,m}(k) = \begin{cases} 1 & (m \text{ is even}), \\ \frac{-ig' \pm \sqrt{4\kappa'^2\cos^2(kL_{CC}) - g'^2}}{\kappa'[1+\exp(i2kL_{CC})]} & (m \text{ is odd}). \end{cases} \quad (14)$$

The absence of an offset for m and t in Eq. (13) means that the initial pulse is excited at the spatial and temporal references, i.e., $m = t = 0$.

To set the spectral function $F_{\pm}(k)$, we perform a variable transformation from an input frequency distribution,

$$F(\Delta\omega, \Delta\omega_0, \sigma_t) = \sqrt{2\pi}\sigma_t \exp\left(-\frac{\sigma_t^2}{2}(\Delta\omega - \Delta\omega_0)^2\right), \quad (15)$$

which corresponds to a temporal Gaussian pulse with a variance σ_t^2 and a central frequency detuning of $\Delta\omega_0$ in free space. Note that $F_{\pm}(k)$ is not Gaussian because of the nonlinear band structure of the considered system, namely,

$$F_{\pm}(k) = F(\Delta\omega, \Delta\omega_0, \sigma_t) \cdot \frac{d\Delta\omega_{\pm}(k)}{dk}. \quad (16)$$

Indeed, $d\Delta\omega_{\pm}(k)/dk$ in Eq. (16) is the group velocity [Eq. (8)], diverging at the phase-transition point. However, the integration represented by Eq. (13) is finite as long as the amplification by the states with imaginary eigenfrequencies in the broken $\mathcal{PT}$ phase (after the $\mathcal{PT}$ symmetry breaking) is avoided. Here, we limit the analysis to the exact $\mathcal{PT}$ phase (before the symmetry breaking). This is because the states in the broken $\mathcal{PT}$ phase have flat real bands ($v_g = 0$) and curved imaginary bands, which only support monochromatic standing waves with amplification and deamplification (see Fig. 3). Furthermore, we focus on a single propagation direction, and hence on the case where the states are pumped with positive group velocities. As a result, the integral ranges for the first and second terms of Eq. (13) can be $[-k_{PT}, 0]$ and $[0, k_{PT}]$, respectively, where k_{PT} is the phase-transition point in $[0, \pi/(2L_{CC})]$. Note that the states with $\Delta\omega_+(k)$ support positive group velocities in the negative wave-number region $[-k_{PT}, 0]$, although this region is omitted in the tight-binding analysis in Secs. III B and III C.

We consider detecting the temporal pulse intensities at $m = 100$, corresponding to a distance of $mL_{CC} = 210$ μm from the excitation point, for both $\mathcal{PT}$-symmetric and conventional empty CROWs. Figs. 5(a) and 5(b) show examples of pulse propagation for different pulse intensity widths of 10 and 100 ps, with their central frequencies at the phase-transition point. With a short input pulse, we can achieve a large relative shift in time by switching between the $\mathcal{PT}$-symmetric and empty CROWs [Fig. 5(a)]. In addition, the pulse broadening in the $\mathcal{PT}$-symmetric CROW is not significant for the propagation distance of 210 μm. However, the maximum peak velocity (ideally

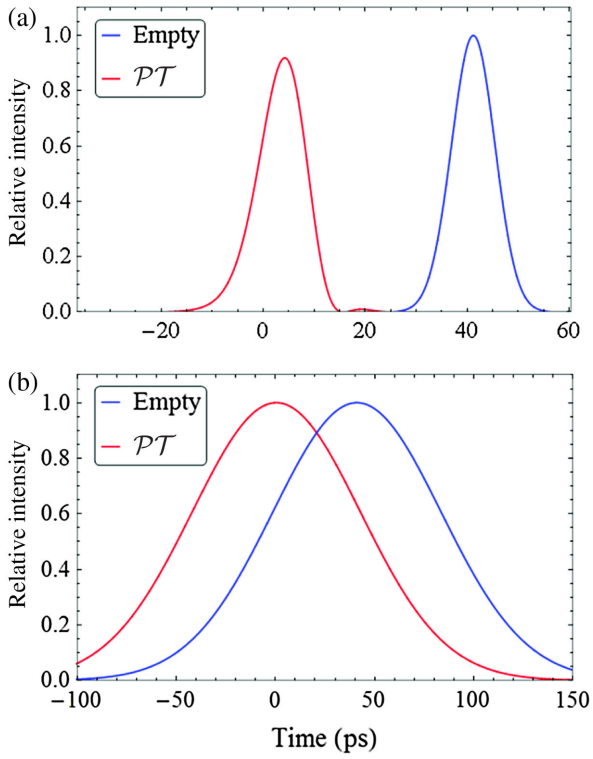

FIG. 5. Examples of the propagation of pulses with the central frequency at the exceptional point and temporal durations of (a) 10 and (b) 100 ps in the $\mathcal{PT}$-symmetric (red lines) and conventional (blue lines) CROWs. $m = 100$. $n_{BH} = 3.54$, $\lambda_0 = 2\pi c/\omega_0 = 1.55$ μm, $\kappa = 2 \times 10^{-3}$, $g = 405$ cm^{-1} [satisfying Eq. (10)].

corresponding to the group velocity) is limited because it is affected by the broad spectral width. A longer pulse [Fig. 5(b)] has a narrower spectrum and hence enables a faster peak velocity. However, it is more difficult to detect the absolute time delay caused by the propagation in the $\mathcal{PT}$-symmetric CROW and the temporal pulse shift than with the conventional CROW.

Figure 6 shows the dependence of the forward peak velocity on the central frequency for different temporal pulse durations. The maximum peak velocity is obtained with the central frequency at the exceptional point for both the $\mathcal{PT}$-symmetric CROW (shown as curves with markers) and the conventional empty CROW (the dashed-dotted line). The peak velocity in the $\mathcal{PT}$-symmetric CROW agrees with the theoretical analysis [Eq. (8)] shown by the dotted curve for detuning approximately larger than the spectral width of the input pulse. On the other hand, it does not diverge around the phase-transition point, $\Delta\omega = 0$. This is very probably because the peak is delayed by the third and higher-order dispersion, and the effect is more significant for pulses with broader spectral widths, and hence shorter temporal durations. However, a long pulse can show superluminal peak propagation there, as shown by the example for 100 ps in Fig. 5(b), which achieves 4.66×10^8 km/s. The ratios of the maximum velocity in

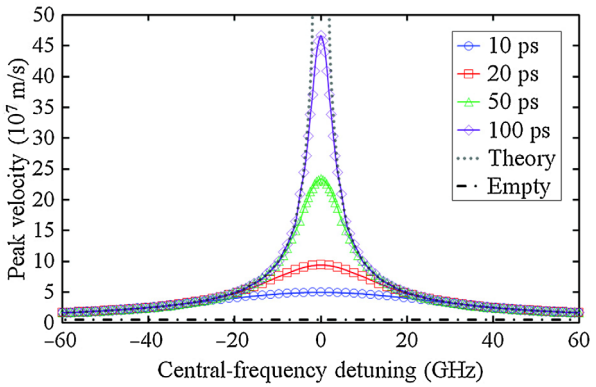

FIG. 6. Dependence of forward peak velocity of the pulse on its central frequency. Lines with markers are for the $\mathcal{PT}$-symmetric CROW with different input pulse widths. The dotted line shows the theoretical group velocity for the $\mathcal{PT}$-symmetric CROW. The dashed-dotted line is the group velocity of the empty CROW. The parameters are the same as those in Fig. 5.

the $\mathcal{PT}$-symmetric CROW to that in the conventional CROW for $\Delta\omega = 0$ are 9.72, 18.4, 45.4, and 91.3 for 10-, 20-, 50-, and 100-ps pulses, respectively. Meanwhile, as shown in the next section, the group velocity around the exceptional point is decreased by the radiation loss of the device; thus, a low-loss system will also be needed to keep the controllability of the velocity.

It is noteworthy that if we excite the bands with positive and negative group velocities at the same time, a pair of pulses propagating in the opposite directions is formed. This bidirectional excitation can cause a sharp decrease in the apparent pulse velocity around the exceptional point, which might be seen in previous work for honeycomb photonic lattices [30]. The velocity drop might also indicate the flux velocity cancellation discussed in Ref. [19]. To achieve the sole advancing pulse in our simulation above within the scope of the exact $\mathcal{PT}$ phase, the system needs the selectivity of the propagation direction (i.e., the wave number) and frequency in the excitation. The way to realize this selectivity is nontrivial and to be explored further.

IV. NUMERICAL SIMULATION FOR PHOTONIC-CRYSTAL STRUCTURES

A. Theoretical model

In this section, we show and discuss the result of a simulation of realistic photonic-crystal structures based on the finite-element method. We perform an eigenfrequency analysis of the Maxwell equation mainly on two-dimensional structures to explore basic features. We employ a three-dimensional numerical simulation to confirm the main result, compare the devices in two and three dimensions, and estimate the actual device specifications.

Figures 7(a) and 7(b) show the simulated three-dimensional device structure and its two-dimensional top view, respectively. Here, two BHM cavities with dimensions

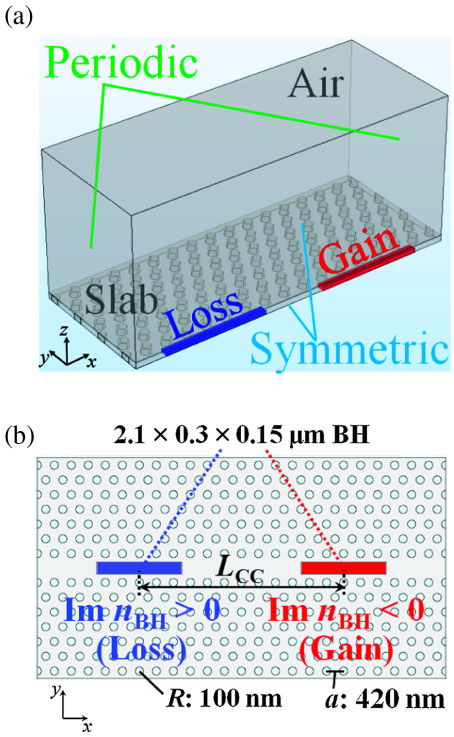

FIG. 7. (a) Schematic of the simulated device structure in three dimensions. (b) Top view of (a) without the symmetry boundary on the x-z plane, which corresponds to the considered two-dimensional structure.

of $2.1 \times 0.3 \times 0.15$ μm undergo loss ($\mathrm{Im}n_{\mathrm{BH}} > 0$) and gain ($\mathrm{Im}n_{\mathrm{BH}} < 0$) via the imaginary parts of their input material indices ($\mathrm{Im}n_{\mathrm{BH}}$). The lattice constant of the triangular photonic crystal is $a = 420$ nm, and the airhole radius is $R = 100$ nm. Seven rows of airholes are aligned on each side of the line defect. As shown in Fig. 7(a), symmetric boundary planes are placed along with the center of the line defect and on the bottom of the structure in the simulation, while Fig. 7(b) shows the entire two-dimensional unit cell for reference. The periodic boundary condition is set to enable us to analyze the band structure of infinite pairs of cavities. Perfectly matched layers (PMLs) are attached outside the main structure. Two widths W of the two-dimensional line-defect part, $W = 0.98W_0$ and $W = 0.85W_0$, are considered. Here, W is defined as the distance between the airhole rows on the upper and lower sides of the waveguide, and $W_0 = \sqrt{3}a$. We find that narrowing the line defect improves the total Q factor of the leaky lower CROW supermode. This effect is much more significant in three-dimensional structures than in two-dimensional ones. For the two-dimensional system, as in Fig. 7(b), we use the effective refractive indices $n_{\mathrm{sl}} = 2.59$ for the InP slab and $\mathrm{Re}n_{\mathrm{BH}} = 2.77$ for the In-Ga-As-P BHM cavities [22]. In the three-dimensional simulation, the thickness of the slab is 250 nm, and the material indices $n_{\mathrm{sl}} = 3.17$ and $\mathrm{Re}n_{\mathrm{BH}} = 3.54$ are introduced. In the vertical direction, air layers are sandwiched between the slab and the PMLs. Typical device

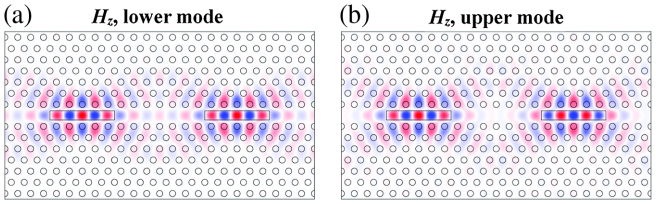

FIG. 8. H_z fields of the considered supermodes for the empty CROW ($\mathrm{Im}n_{\mathrm{BH}} = 0$). The (a) lower and (b) upper modes have in-phase and out-of-phase couplings, respectively. $k = 0$.

parameters $\{Q, \kappa', L_{\mathrm{CC}}\}$ obtained in our simulation are $\{10^6, 130\ \mathrm{GHz}, 3.4\ \mu\mathrm{m}\}$ and $\{5 \times 10^5, 50\ \mathrm{GHz}, 3.4\ \mu\mathrm{m}\}$ in two and three dimensions, respectively. The cavity couplings here are smaller than that in a Si system [3]. This difference might diminish values of v_g obtained in this section compared with our previous tight-binding analysis. Couplings in a diagonal direction [7] will be available to increase κ', although those are beyond the scope of this work.

Figure 8 shows the considered eigenmodes for the empty CROW ($\mathrm{Im}n_{\mathrm{BH}} = 0$) in terms of the out-of-plane component of the magnetic field $H_z(x, y)$. Here, the ground even mode in terms of H_z is excited and well confined in the cavities. In the lower-band eigenmode [Fig. 8(a)], an antinode is formed in the middle of the line-defect part, and the two BHM cavity modes are in phase. On the other hand, the upper-band mode [Fig. 8(b)] has a node at the center of the line-defect and out-of-phase cavity modes.

When the cavities are close, the second- and higher-order couplings are not negligible and the resultant band structure verges on that of the line-defect waveguide of the BH medium. To fit the simulation data, we apply the Rice-Mele model [29,31], which covers up to the second nearest-neighbor coupling,

$$\omega_{\pm}(k) = \omega_0 - 2\rho\cos(2L_{\mathrm{CC}}k + \phi) \pm \sqrt{-g'^2 + 2\kappa'^2[1 + \cos(2L_{\mathrm{CC}}k)]}. \quad (17)$$

Here, ω_0 is the single-cavity resonance frequency. ρ and ϕ are the second nearest-neighbor coupling rate and phase, respectively. Note that the second nearest-neighbor coupling—that is, the second term in Eq. (17)—adds only a small change in v_g and does not impede its divergence at the transition point. If we assume that the data obey Eq. (17), all of the parameters can be determined without any free fitting parameters. κ', ρ, and ϕ are obtained from the eigenfrequencies for $(k, \mathrm{Im}n_{\mathrm{BH}}) = (0, 0), (\pi/(2L_{\mathrm{CC}}), 0)$ (empty CROW). The ratio between $\mathrm{Im}n_{\mathrm{BH}}$ and g' is estimated by using the data points for $k = 0$ and various $\mathrm{Im}n_{\mathrm{BH}}$ values.

B. $\mathcal{PT}$ phase transition by loss and gain

We first investigate the complex eigenfrequency dependence on the magnitude of the gain and loss in a two-dimensional device with $L_{\mathrm{CC}} = 8a$. Here, we fix the Bloch wave number to the middle of the band for $k > 0$, i.e., $k = \pi/(4L_{\mathrm{CC}})$, to find the gain and loss rates that give the largest group velocities around the phase transition within the first-order limits (see Sec. III C). Figure 9(a) shows the wavelength λ (the black curve) and the system gain or loss rate (the red curve), which are calculated with $\mathrm{Re}\omega_{\pm}(k)$ and $\mathrm{Im}\omega_{\pm}(k)$, respectively. Positive and negative $\mathrm{Im}\omega_{\pm}(k)$ values correspond to the system loss and gain. The markers show the result of the numerical simulation, and the curves are drawn with Eq. (17). We find that Eq. (17) with the calculated device parameters does not reproduce the simulation data well in terms of the position of the phase-transition point. We attribute this deviation to the higher-order couplings and then reduce κ' by 4% to take it into account approximately within the scope of the theoretical model. With this shift, the data points agree well with the dependence on g' in Eq. (17) without any other fitting parameters. The result presents a sharp $\mathcal{PT}$ phase transition from real to imaginary detuning eigenvalues $\omega_{\pm}(k) - \omega_0$ around $\lambda \approx 1587.25$ nm. Here, the material imaginary index to reach the transition is $\mathrm{Im}n_{\mathrm{BH}} = \pm 0.0103$, and the corresponding spatial loss and gain rates are $g_{\mathrm{BH}} = \pm 823\ \mathrm{cm}^{-1}$. This means that the $\mathcal{PT}$ phase

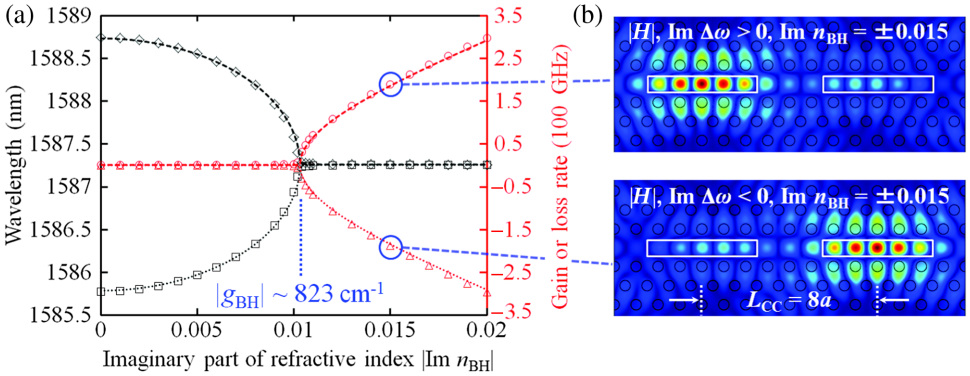

FIG. 9. (a) Dependence of the eigenwavelength (black curves) and system gain or loss rate (red curves) on the imaginary part of the cavity refractive index $|\mathrm{Im}n_{\mathrm{BH}}|$ at the middle of the band for $k > 0$: $k = \pi/(4L_{\mathrm{CC}})$. Markers show the simulated data points. Curves are based on Eq. (17), with $\omega_0 = 189.0$ THz, $\kappa' = 124.0$ GHz, $\rho = 16.17$ GHz, $\phi = 0.008730$ rad, and $g' = 1.700 \times 10^4 \mathrm{Im}n_{\mathrm{BH}}$ GHz. (b) Magnitudes of the magnetic fields for the eigenmodes with $\mathrm{Im}n_{\mathrm{BH}} = \pm 0.015$. $L_{\mathrm{CC}} = 8a$, in two dimensions.

transition for a large change in v_g will be achievable with a realistic carrier-injection gain in III-V quantum wells [32]. Figure 9(b) depicts the norm of the magnetic field for the eigenmodes after phase transition, with $\mathrm{Im}n_{\mathrm{BH}} = \pm 0.015$. We see that we can attribute the two states with loss $[\mathrm{Im}\omega_{\pm}(k) > 0]$ and gain $[\mathrm{Im}\omega_{\pm}(k) < 0]$ to the localized modes in the left $(\mathrm{Im}n_{\mathrm{BH}} > 0)$ and right $(\mathrm{Im}n_{\mathrm{BH}} < 0)$ cavities, respectively. Note that the cavity-mode profiles before and at the phase transition are similar to those shown in Fig. 8. This means that the localization effect gradually appears as the imaginary part of the eigenfrequency increases.

C. Band structure and group index for two- and three-dimensional structures

With the gain and loss coefficients inducing the phase transition at $k = \pi/(4L_{\mathrm{CC}})$, we next explore the complex band structure to examine the behavior of the $\mathcal{PT}$ phase transition and the possible group velocity in the wave-number space of realistic systems. Figure 10(a) shows the band curves in terms of the wavelength and the gain or loss rate for a two-dimensional system with $W = 0.98W_0$. The parameters used here are the same as those in Fig. 9. The small deviation between the simulated data points and the theoretical curves can probably be attributed to the insufficient compensation of the effect of the third and higher nearest-neighbor couplings. We use $\mathrm{Im}n_{\mathrm{BH}} = \pm 0.0104$ by considering Fig. 9(a) and successfully observe a $\mathcal{PT}$ phase transition around $k = \pi/(4L_{\mathrm{CC}})$. It is seen that the real band has finite slopes after the phase transition due to hopping propagation via the second nearest-neighbor coupling. Figure 10(b) shows the wavelength-dependent group index $n_g = c/v_g$ for the two-dimensional device. It includes finer data points around the phase transition than in Fig. 10(a). When the n_g of the $\mathcal{PT}$-symmetric CROW is minimal, the ratio of n_g relative to the empty CROW reaches 7.2. Note that the magnitude of v_g itself depends on the coupling κ'.

We find that a narrower line defect results in a faster v_g, probably due to the balanced and high-Q factors of the CROW supermodes. Figures 10(c) and 10(d) show the complex band curves and the group index around the transition point for $W = 0.85W_0$. Here, we have $Q = 1.5 \times 10^6$ for the upper mode and 2.0×10^6 for the lower mode with $k = g = 0$. The coupling rates are increased slightly due to the better field confinement, and the entire band structure appears nearly unchanged, except for the shorter wavelengths resulting from the narrower line defect. However, a closer look at Fig. 10(d) reveals that a smaller n_g of 2.69 is obtained, and this value results in as much as a 19-fold acceleration. Note that the minimum value is slightly below the two-dimensional BH material index $\mathrm{Re}n_{\mathrm{BH}} = 2.77$.

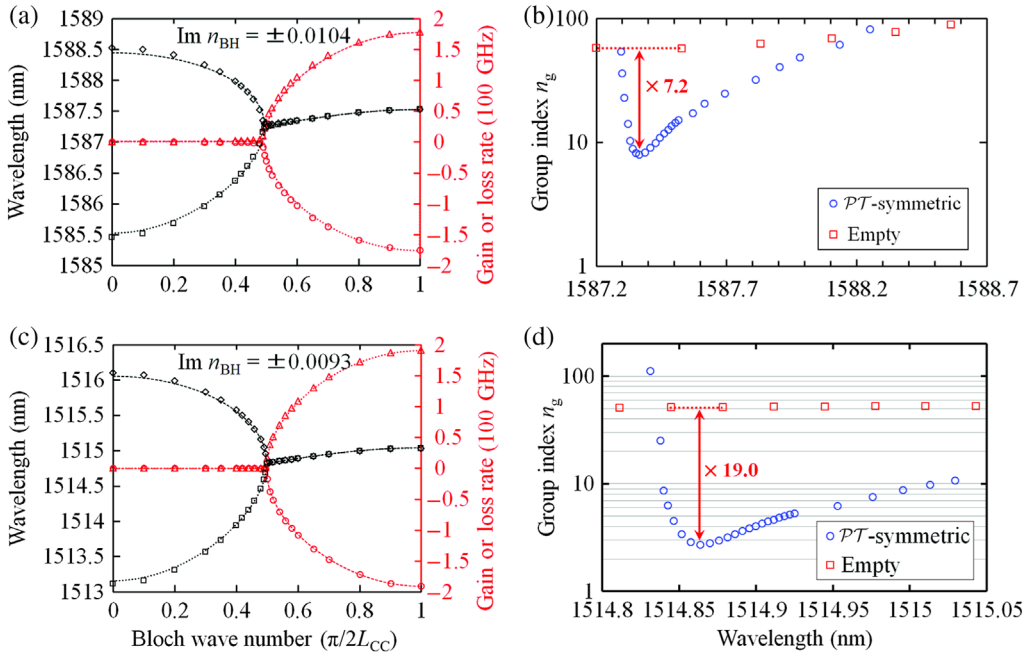

FIG. 10. (a) Complex band structure shown as the eigenwavelength (black curves) and gain or loss rate (red curves—positive for loss, negative for gain) in a two-dimensional device with a line-defect width of $0.98W_0$. Markers indicate the simulated data. The parameters for the theoretical curves are the same as those in Fig. 9. (b) Dependence of the group index on the wavelength in the same two-dimensional device. (c) Band curves of a two-dimensional device with a narrower line defect $W = 0.85W_0$. The dashed lines indicate theoretical curves with $\omega_0 = 198.0$ THz, $\kappa' = 134.340$ GHz, $\rho = -14.26$ GHz, $\phi = 0.007432$ rad, and $g' = 2.0503 \times 10^4 \mathrm{Im}n_{\mathrm{BH}}$ GHz. Here, the calculated κ' is decreased by 3.5% to fit the simulated data points. (d) Fine data of the group index around the phase-transition wavelength for a two-dimensional device with the line-defect width of $0.85W_0$. The minimum index $n_g = 2.69$ is slightly below the cavity material effective index $\mathrm{Re}n_{\mathrm{BH}} = 2.77$.

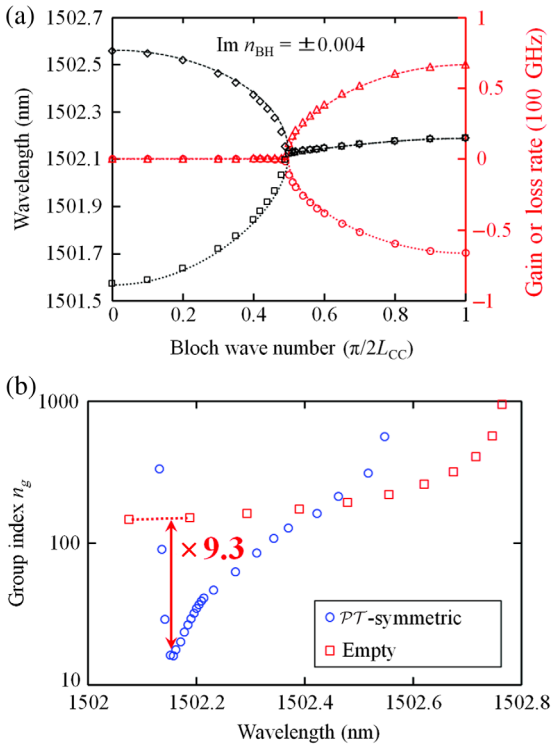

FIG. 11. (c) Band structure for a three-dimensional device with $L_{CC} = 8a$ and a line-defect width of $0.85W_0$. $\omega_0 = 199.7$ THz, $\kappa' = 46.87$ GHz, $\rho = -4.089$ GHz, $\phi = -0.006088$ rad, and $g' = 1.661 \times 10^4 \mathrm{Im} n_{BH}$ GHz for theoretical curves (the dashed lines). (d) Group index versus the eigenwavelength in the same three-dimensional device.

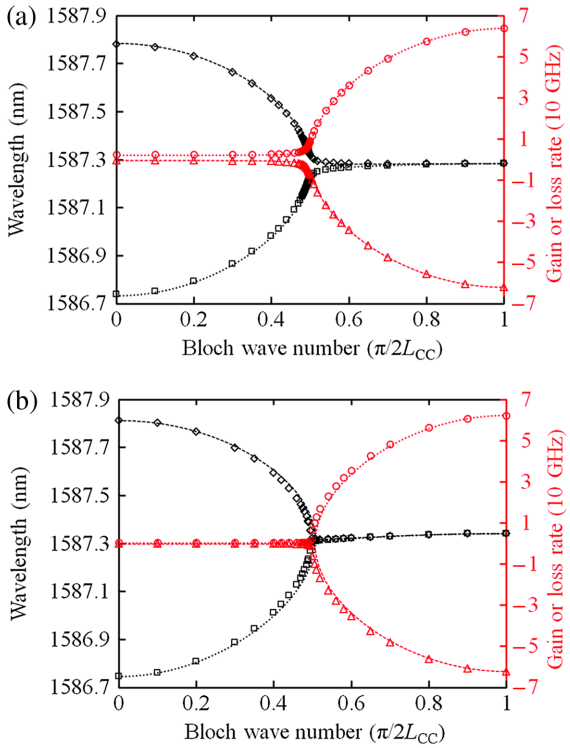

FIG. 12. Complex band curves for two-dimensional devices with different numbers of rows of airholes for photonic crystals, namely, different system Q factors. (a) 7 rows and (b) 15 rows on both sides of the line defect. (a) shows the band smoothing caused by significant radiation loss, and the enhancement of v_g is limited. In (b), a sharp phase-transition structure is restored by a larger Q factor. $L_{CC} = 10a$, and the line-defect width is 0.98 W_0.

Figures 11(a) and 11(b) show the complex band structure and the group index of a three-dimensional device with $W = 0.85W_0$. Its coupling rates, including higher nearest-neighbor coupling rates, are smaller than those for two-dimensional systems because of the radiation loss in the z direction. Thus, the data points in Fig. 11(c) agree well with the theoretical curves, assuming Eq. (17) (without any parameter adjustment). The CROW bandwidth is about 1 nm, and the magnitude of the applied loss and gain is 334.6 cm^{-1}. In Fig. 11(b), we have a relatively large minimum index of 15.91 due to the small coupling rates. However, the index n_g shows a steep change around the phase transition and hence gives a large maximum ratio in n_g of 9.3 compared to the empty CROW.

D. Band smoothing around the phase transition

As previously seen, the group velocity for the realistic photonic-crystal structure does not exhibit divergent behavior despite the fine data points under the periodic boundary condition. This is because the band around the phase transition is smoothed by the field decay from the system. Figures 12(a) and 12(b) depict the complex band curves for the two-dimensional devices with 7 and 15 rows of photonic-crystal airholes, respectively. Here, the cavity spacing is larger, $L_{CC} = 10a$; thus, the couplings are smaller than those in the previous two-dimensional examples. In Fig. 12(a), the sharp phase transition is lost due to the radiation loss and weak coupling, and the minimum n_g in the $\mathcal{PT}$-symmetric CROW is as large as 35.7. At this wavelength, there is only a 3.4-fold change in n_g compared to the empty CROW. The Q factors of the upper and lower CROW supermodes for $k = g = 0$ are 5.0×10^4 and 8.8×10^5, meaning that there is a low-Q state and imbalance of the loss in the supermodes. As shown in Fig. 12(b), a stronger confinement of light in the system with more airholes restores the large v_g around the transition. Here, the minimum n_g and the maximum group-index ratio are 12.7 and 10.3, respectively. Nevertheless, the improved Q factors are 2.9×10^5 and 1.4×10^8; thus, there is still a large difference between them.

In our system, disproportionate Q factors in the supermodes, hampering a large group velocity around the transition, stem from the interference of the evanescent fields. This means that the gain in the BHM cavities cannot compensate for the radiation of the superposed evanescent fields to the outside the structure. This effect is expressed by the non-self-conjugate complex-coupling terms, which

were phenomenologically considered [25] and then confirmed theoretically and experimentally [26] in the context of coupled waveguides. We can introduce this effect by the replacement of κ'^2 with $\kappa'^2 \exp(i\theta)$ in Eq. (6). Indeed, $\theta = 0.02024$ is used in the theoretical curves in Fig. 12(a), which agree well with the data points. Such a non-Hermitian term breaks the unitarity—and hence the photon-number conservation—in the time evolution of the effective system Hamiltonian. Thus, it can be a reason for additional loss in our system and detrimental effects. We emphasize that Ref. [26] focuses on the material absorption in the waveguide cores and the surrounding medium, but the radiation loss in our system (caused by the additional system-reservoir coupling [33]) behaves equivalently. This point is implied in the experiment of Ref. [26] using scattering loss and is indicated by nearly cosinusoidal imaginary bands obtained in the case of our conventional CROWs with low Q and no material gain or loss.

It is noteworthy that such a complex-coupling component is beyond the limits of the standard tight-binding model discussed in Sec. III. However, evanescent waves come from the cavity decay; thus, this term would be implicitly dependent on the cavity Q factor. If we assume that the complex-coupling rate has the same order of the cavity decay rate, the approximate single-cavity Q factor showing significant band smoothing would be $\omega_0/(2\sqrt{\kappa'^2 \sin\theta}) \sim 10^4$. This result supports the loss magnitude of the low-Q supermodes in Fig. 12(a).

In the supermode where the evanescent fields outside the BH cavities are enhanced, the decay is significant. When the evanescent fields are canceled, however, the loss is small while the coupling is maintained. A narrow line defect contributes to the balanced high-Q factors of the CROW modes, and hence to a fast v_g around the phase transition, probably because it broadens the mode gap between the CROW and the photonic crystal. Note that the defect modification does not change the band structure of the surrounding photonic crystal.

Basically, three-dimensional structures are more likely to suffer from band smoothing than two-dimensional systems because of the loss in the vertical direction. As shown in Fig. 11, however, narrowing the line defect in the device largely suppresses this effect, which is significant otherwise. Our design will hence open up the possibility of the experimental realization of $\mathcal{PT}$-symmetric cavity lattices maintaining sharp exceptional-point behavior, which will contribute to group-velocity control and also other phenomena, such as unidirectional reflection and nonlinear optical isolation.

V. DISCUSSION

Here, we discuss the design and the setting of the $\mathcal{PT}$-symmetric CROW described in this study. First, in Sec. III we anticipated that a larger nearest-neighbor coupling rate κ would lead to a faster v_g and a smaller GVD. On the other hand, a larger magnitude g of gain and loss is needed to achieve the condition for the maximum v_g around the phase transition [Eq. (10)]. Our simulation result shows that the required g for the three-dimensional devices with $L_{CC} = 2a$, $3a$, and $4a$ are 460.1, 334.6, and 110.4 cm^{-1}, respectively. These values are typical in reports for other photonic devices [15,34], and thus will also be realizable in our devices. However, we have to design the cavity interval L_{CC} with caution. A long L_{CC} results in a small κ and induces significant band-smoothing effects. On the other hand, a short L_{CC} complicates the band structure due to large higher-order couplings, in addition to the need for a large g.

Finally, we mention the literature of ways to keep the $\mathcal{PT}$ symmetry in realistic systems. A recent theoretical report [35] showed that the gain-induced dispersion in coupled GaAs waveguide cores could wash out the phase change itself, as well as the singularity. Here, the mode index detuning caused by the structural asymmetry and imbalanced gain and loss in the waveguides are introduced to restore their $\mathcal{PT}$-symmetric behavior. As the detuning of constituent waveguides has been examined to dominate the imaginary part of the coupling and heal the singularity [25], the radiation loss might conversely work as a dispersion and detuning compensator, although that prospect is beyond the scope of this paper. In a future experiment, slightly detuned cavity arrays might be picked for small system demonstrations. Delicate injection-current control, including biased pumping, will also be considered at that time.

VI. CONCLUSION

In this paper, we propose a $\mathcal{PT}$-symmetric CROW based on buried heterostructure photonic-crystal nanocavities and study theoretically its application for controlling transport properties. Using the one-dimensional tight-binding model, we derive analytical expressions of the frequency dependence of its group velocity and group-velocity dispersion. Within the limits of this first-order approximation, the group velocity diverges, while the group-velocity dispersion converges at the $\mathcal{PT}$ phase-transition point, showing good potential for the device. Here, the condition for the maximum velocity and the minimum group-velocity dispersion around the transition point is the same. In this case, the velocity is enhanced and the dispersion is suppressed, depending on the square of the cavity coupling rate. An estimation of the system temporal response to input pulses shows that a pulse duration of 10 ps is short enough to detect a boost by switching between conventional and $\mathcal{PT}$-symmetric CROWs with a length of 210 μm, while the ratio of their pulse peak velocities is relatively limited. A longer duration, and hence a narrower spectral distribution of the pulse, provides us with a higher upper limit of the velocity around the $\mathcal{PT}$ phase-transition point, although a judicious pulse excitation setup could be required in an experiment. In a device simulation based on

the finite-element method, we successfully observe the $\mathcal{PT}$ phase transition in the proposed photonic-crystal structures with controlled amplification and absorption. In the parameter range we examine, the second nearest-neighbor coupling is not negligible and it bends the band curves after the phase transition. For three-dimensional devices, loss and gain magnitudes with an order of 100 cm^{-1} are sufficient to satisfy the condition for the maximum group velocity around the phase transition. A problem with achieving a large group velocity in the actual device is the band smoothing that destroys the exceptional-point singularity. Our simulation result indicates that the main reason for this imperfection is the decay of the interfering evanescent waves from the pairs of cavities, which can be considered the imaginary part of the cavity coupling rate. Increasing and balancing the Q factors of the CROW supermodes with an appropriate design opens up the possibility of wide-range controllability of optical transport, potentially including superluminal light propagation.

ACKNOWLEDGMENTS

We thank Akihiko Shinya, Kengo Nozaki, Masato Takiguchi, and Shota Kita for the fruitful discussions. This work was supported by the Japan Science and Technology Agency (JST) through the Core Research for Evolutionary Science and Technology (CREST) program under Grant No. JPMJCR15N4.

[1] A. Yariv, Y. Xu, R. K. Lee, and A. Scherer, Coupled-resonator optical waveguide: A proposal and analysis, Opt. Lett. **24**, 711 (1999).

[2] Y. Xu, R. K. Lee, and A. Yariv, Propagation and second-harmonic generation of electromagnetic waves in a coupled-resonator optical waveguide, J. Opt. Soc. Am. B **17**, 387 (2000).

[3] M. Notomi, E. Kuramochi, and T. Tanabe, Large-scale arrays of ultrahigh-Q coupled nanocavities, Nat. Photonics **2**, 741 (2008).

[4] N. Matsuda, T. Kato, K. Harada, H. Takesue, E. Kuramochi, H. Taniyama, and M. Notomi, Slow light enhanced optical nonlinearity in a silicon photonic crystal coupled-resonator optical waveguide, Opt. Express **19**, 19861 (2011).

[5] Y. Liu, Z. Wang, M. Han, S. Fan, and R. Dutton, Mode-locking of monolithic laser diodes incorporating coupled-resonator optical waveguides, Opt. Express **13**, 4539 (2005).

[6] C. Agger, T. S. Skovgård, N. Gregersen, and J. Mørk, Modeling of mode-locked coupled-resonator optical waveguide lasers, IEEE J. Quantum Electron. **46**, 1804 (2010).

[7] E. Kuramochi, N. Matsuda, K. Nozaki, H. Takesue, and M. Notomi, Over-1mm-long wideband on-chip slowlight waveguides realized by 1,000 coupled L3 nanocavities, in *Proceedings of the 2015 Conference on Lasers and Electro-Optics (CLEO 2015), San Jose, 2015* (Optical Society of America, Washington, D.C., 2015).

[8] C. M. Bender and S. Boettcher, Real Spectra in Non-Hermitian Hamiltonians Having $\mathcal{PT}$ Symmetry, Phys. Rev. Lett. **80**, 5243 (1998).

[9] K. G. Makris, R. El-Ganainy, D. N. Christodoulides, and Z. H. Musslimani, Beam Dynamics in $\mathcal{PT}$ Symmetric Optical Lattices, Phys. Rev. Lett. **100**, 103904 (2008).

[10] A. Guo, G. J. Salamo, D. Duchesne, R. Morandotti, M. Volatier-Ravat, V. Aimez, G. A. Siviloglou, and D. N. Christodoulides, Observation of $\mathcal{PT}$-Symmetry Breaking in Complex Optical Potentials, Phys. Rev. Lett. **103**, 093902 (2009).

[11] C. E. Rüter, K. G. Makris, R. El-Ganainy, D. N. Christodoulides, M. Segev, and D. Kip, Observation of parity-time symmetry in optics, Nat. Phys. **6**, 192 (2010).

[12] A. Regensburger, C. Bersch, M.-A. Miri, G. Onishchukov, D. N. Christodoulides, and U. Peschel, Parity-time synthetic photonic lattices, Nature (London) **488**, 167 (2012).

[13] Z. Lin, H. Ramezani, T. Eichelkraut, T. Kottos, H. Cao, and D. N. Christodoulides, Unidirectional Invisibility Induced by $\mathcal{PT}$-Symmetric Periodic Structures, Phys. Rev. Lett. **106**, 213901 (2011).

[14] L. Feng, Y.-L. Xu, W. S. Fegadolli, M.-H. Lu, J. E. B. Oliveira, V. R. Almeida, Y.-F. Chen, and A. Scherer, Experimental demonstration of a unidirectional reflectionless parity-time metamaterial at optical frequencies, Nat. Mater. **12**, 108 (2013).

[15] L. Feng, Z. J. Wong, R.-M. Ma, Y. Wang, and X. Zhang, Single-mode laser by parity-time symmetry breaking, Science **346**, 972 (2014).

[16] H. Hodaei, M.-A. Miri, M. Heinrich, D. N. Christodoulides, and M. Khajavikhan, Parity-time-symmetric microring lasers, Science **346**, 975 (2014).

[17] M. Wimmer, A. Regensburger, M.-A. Miri, C. Bersch, D. N. Christodoulides, and U. Peschel, Observation of optical solitons in $\mathcal{PT}$-symmetric lattices, Nat. Commun. **6**, 7782 (2015).

[18] O. Vázquez-Candanedo, J. C. Hernández-Herrejón, F. M. Izrailev, and D. N. Christodoulides, Gain- or loss-induced localization in one-dimensional $\mathcal{PT}$-symmetric tight-binding models, Phys. Rev. A **89**, 013832 (2014).

[19] H. Schomerus and J. Wiersig, Non-Hermitian-transport effects in coupled-resonator optical waveguides, Phys. Rev. A **90**, 053819 (2014).

[20] B. Peng, S. K. Özdemir, F. Lei, F. Monifi, M. Gianfreda, G. L. Long, S. Fan, F. Nori, C. M. Bender, and L. Yang, Parity-time-symmetric whispering-gallery microcavities, Nat. Phys. **10**, 394 (2014).

[21] L. Chang, X. Jiang, S. Hua, C. Yang, J. Wen, L. Jiang, G. Li, G. Wang, and M. Xiao, Parity-time symmetry and variable optical isolation in active-passive-coupled microresonators, Nat. Photonics **8**, 524 (2014).

[22] S. Matsuo, A. Shinya, T. Kakitsuka, K. Nozaki, T. Segawa, T. Sato, Y. Kawaguchi, and M. Notomi, High-speed ultra-compact buried heterostructure photonic-crystal laser with 13 fJ of energy consumed per bit transmitted, Nat. Photonics **4**, 648 (2010).

[23] K. Takeda, T. Sato, A. Shinya, K. Nozaki, W. Kobayashi, H. Taniyama, M. Notomi, K. Hasebe, T. Kakitsuka, and S. Matsuo, Few-fJ/bit data transmissions using directly modulated lambda-scale embedded active region photonic-crystal lasers, Nat. Photonics **7**, 569 (2013).

[24] S. Matsuo, T. Sato, K. Takeda, A. Shinya, K. Nozaki, E. Kuramochi, H. Taniyama, M. Notomi, T. Fujii, K. Hasebe, and T. Kakitsuka, Photonic crystal lasers using wavelength-scale embedded active region, J. Phys. D **47**, 023001 (2014).

[25] H. Benisty, C. Yan, A. Degiron, and A. Lupu, Healing near-$\mathcal{PT}$-symmetric structures to restore their characteristic singularities: Analysis and examples, J. Lightwave Technol. **30**, 2675 (2012).

[26] M. Golshani, S. Weimann, Kh. Jafari, M. K. Nezhad, A. Langari, A. R. Bahrampour, T. Eichelkraut, S. M. Mahdavi, and A. Szameit, Impact of Loss on the Waveguide Dynamics in Photonic Waveguide Lattices, Phys. Rev. Lett. **113**, 123903 (2014).

[27] Y. Yamamoto and N. Imoto, Internal and external field fluctuations of a laser oscillator: Part I—Quantum mechanical Langevin treatment, IEEE J. Quantum Electron. **22**, 2032 (1986).

[28] D. T. Nichols and H. G. Winful, The effect of nonlinear gain on the stability of evanescently coupled semiconductor laser arrays, J. Appl. Phys. **73**, 459 (1993).

[29] S. Longhi, Convective and absolute $\mathcal{PT}$-symmetry breaking in tight-binding lattices, Phys. Rev. A **88**, 052102 (2013).

[30] A. Szameit, M. C. Rechtsman, O. Bahat-Treidel, and M. Segev, $\mathcal{PT}$-symmetry in honeycomb photonic lattices, Phys. Rev. A **84**, 021806(R) (2011).

[31] M. J. Rice and E. J. Mele, Elementary Excitations of a Linearly Conjugated Diatomic Polymer, Phys. Rev. Lett. **49**, 1455 (1982).

[32] S. Y. Hu, S. W. Corzine, K.-K. Law, D. B. Young, A. C. Gossard, L. A. Coldren, and J. L. Merz, Lateral carrier diffusion and surface recombination in InGaAs/AlGaAs quantum-well ridge-waveguide lasers, J. Appl. Phys. **76**, 4479 (1994).

[33] H. J. Carmichael, *Statistical Methods in Quantum Optics 1: Master Equations and Fokker-Planck Equations* (Springer, Berlin, 1999).

[34] S. Ek, P. Lunnemann, Y. Chen, E. Semenova, K. Yvind, and J. Mork, Slow-light-enhanced gain in active photonic crystal waveguides, Nat. Commun. **5**, 5039 (2014).

[35] N. B. Nguyen, S. A. Maier, M. Hong, and R. F. Oulton, Recovering parity-time symmetry in highly dispersive coupled optical waveguides, New J. Phys. **18**, 125012 (2016).